

# Micro-tearing modes in the mega ampere spherical tokamak

D J Applegate<sup>1</sup>, C M Roach<sup>2</sup>, J W Connor<sup>2</sup>, S C Cowley<sup>3</sup>, W Dorland<sup>4</sup>,  
R J Hastie<sup>2</sup> and N Joiner<sup>5</sup>

<sup>1</sup> Department of Physics, University of York, UK

<sup>2</sup> EURATOM/UKAEA Fusion Association, Culham Science Centre, UK

<sup>3</sup> Department of Physics and Astronomy, UCLA, USA

<sup>4</sup> Department of Physics, University of Maryland, USA

<sup>5</sup> Department of Physics and Engineering Physics, University of Saskatchewan, Canada

Received 2 February 2007, in final form 2 April 2007

Published 2 July 2007

Online at [stacks.iop.org/PPCF/49/1113](http://stacks.iop.org/PPCF/49/1113)

## Abstract

Recent gyrokinetic stability calculations have revealed that the spherical tokamak is susceptible to tearing parity instabilities with length scales of a few ion Larmor radii perpendicular to the magnetic field lines. Here we investigate this ‘micro-tearing’ mode in greater detail to uncover its key characteristics and compare it with existing theoretical models of the phenomenon. This has been accomplished using a full numerical solution of the linear gyrokinetic–Maxwell equations. Importantly, the instability is found to be driven by the free energy in the electron temperature gradient as described in the literature. However, our calculations suggest it is not substantially affected by either of the destabilizing mechanisms proposed in previous theoretical models. Instead the instability is destabilized by interactions with magnetic drifts and the electrostatic potential. Further calculations reveal that the mode is not significantly destabilized by the flux surface shaping or the large trapped particle fraction present in the spherical tokamak. Its prevalence in spherical tokamak plasmas is primarily due to the higher value of plasma  $\beta$  and the enhanced magnetic drifts due to the smaller radius of curvature.

(Some figures in this article are in colour only in the electronic version)

## 1. Introduction

The linear tearing instability, described by Furth *et al* [1], progresses by relaxing a sheared magnetic field into a lower energy magnetic island structure. Importantly, the energy released from this process decreases as a function of mode number, which prevents the formation of shorter wavelength tearing instabilities. However, later calculations by Hazeltine *et al* [2] demonstrated that the linear tearing instability could also be driven by an electron temperature

gradient in slab geometry. This new mechanism may enable the tearing instability to exist at higher mode numbers, giving rise to the term ‘micro-tearing mode.’

For a given toroidal mode number  $n$ , the distance between adjacent rational surfaces is  $\delta r = 1/nq'$ , where  $q'$  is the radial derivative of the safety factor  $q$ . Consequently, the chains of islands formed by micro-tearing instabilities are in close proximity and may overlap producing a stochastic field line structure. When this occurs, the electrons are no longer confined to equilibrium flux surfaces and are able to move radially by moving along the perturbed field lines. This process can produce significant electron heat transport, which could explain the high ratios of  $T_i/T_e$  measured in a number of spherical tokamak (ST) plasmas (including those from START and NSTX [3, 4]).

The drive mechanism for this micro-tearing instability can be explained in terms of the parallel thermal force [5]. This force is due to the different frictional forces experienced by electrons travelling in opposite directions along a parallel temperature gradient and has a magnitude given by

$$F_{\text{th}} \sim -n_e \frac{\mathbf{B} \cdot \nabla T_e}{|\mathbf{B}|}, \quad (1)$$

where  $n_e$  and  $T_e$  are the electron density and temperature, respectively. The parallel current resulting from this force will produce a magnetic field perturbation  $\tilde{\mathbf{B}}$ . Instability then arises if this field perturbation aligns with an equilibrium electron temperature gradient  $\nabla T_e$ .

The later paper by Hassam [5], uses a second order Chapman–Enskog expansion of the fluid equations to recover a similar solution. This work notes that the time-dependent thermal force is also important to the drive mechanism of the micro-tearing instability. (This time-dependent force is not present in first order Chapman–Enskog fluid theories, so the Braginskii equations [6] are unable to recover the instability.)

Drake and Lee [7] expand on the work of Hazeltine *et al* [2], by carefully defining three collisional limits in which the slab/cylindrical micro-tearing instability can be analytically treated: the collisional regime, where  $\bar{v}_e \gg \omega$ ; the semi-collisional regime, defined by  $\bar{v}_e > \omega$  and  $\bar{v}_e > k_{\parallel}^2 v_{\text{th}e}^2 / \omega$  (nb. perturbations take the form  $\tilde{\xi} = \hat{\xi} e^{i(m\theta - n\phi - \omega t)}$  such that  $k_{\parallel} = (m - nq)/Rq$ ); and finally the collisionless regime where  $\bar{v}_e \ll \omega$ . In these expressions,  $v_{\text{th}e}$  is the thermal velocity of electrons,  $\omega$  is the mode frequency,  $k_{\parallel}$  is the wavenumber of the mode parallel to the equilibrium field lines and  $\bar{v}_e = (4\pi n_e e^4 \ln \lambda) / ((2T_e)^{3/2} m_e^{1/2})$  determines the collision rate experienced by electrons. Hot tokamak plasmas typically have  $\bar{v}_e \leq \omega$ , which best agrees with the collisionless limit of Drake and Lee. Importantly the thermal force vanishes in this limit, meaning the collisionless *micro-tearing* mode is stable in slab geometry [7, 8] suggesting the micro-tearing mode may not be important in fusion plasmas such as ITER.

However, the paper by Catto and Rosenbluth [9] demonstrates another drive mechanism for the tearing instability in the ITER relevant banana regime ( $\bar{v}_e < \omega_{\text{be}}$  where  $\omega_{\text{be}}$  is the electron bounce frequency). In this limit electrons close to the trapped–passing boundary can easily scatter between the trapped and passing populations. This increases the effective collision rate in a layer around the trapped–passing boundary and allows a destabilizing current to flow. Catto and Rosenbluth [9] have shown this can destabilize the tearing mode in the regime  $\bar{v}_e/\epsilon < \omega$ . In similar spirit, Connor *et al* [10] show the trapped particle driven mode is stable when  $\bar{v}_e/\epsilon > \omega > \bar{v}_e$ .

Importantly, gyrokinetic simulations have identified the micro-tearing mode in a number of ST H-mode plasmas [11–14]. Here we build on these previous calculations with a closer investigation of the instability. In particular, the key characteristics of the instability are uncovered and compared with existing theoretical models of the phenomenon. Section 2

**Table 1.** Global parameters for the MAST equilibrium at  $t = 0.265$  s in MAST discharge #6252. Here  $B_0$  is the toroidal magnetic field on the magnetic axis,  $I_p$  is the plasma current,  $R$  and  $a$  are, respectively, the major and minor radius of the last closed flux surface,  $R_{\text{mag}}$  is the major radius of the magnetic axis.  $P_{\text{beam}}$  is the applied neutral beam heating, and finally  $Z_{\text{eff}} = \sum_s Q_s^2 n_s / n_e$  (where  $s$  labels the ion species and  $Q_s$  is the electric charge of the ion species.).

$B_0$ (T)	$I_p$ (MA)	$R$ (m)	$a$ (m)	$R_{\text{mag}}$ (m)	$P_{\text{beam}}$ (MW)	$Z_{\text{eff}}$
0.458	0.738	0.816	0.558	0.901	1.67	1.5

**Table 2.** Important parameters for the poloidal flux surface  $\psi_n = 0.4$ .  $T_e$  and  $T_i$  are the electron and ion temperatures,  $P$  is the plasma pressure, while  $n$  gives the number density for both ions and electrons. The normalized gradient of a quantity  $x$  is defined as  $a/L_x = (-1/x)(dx/d\psi_n)$ , while  $\hat{s} = (\psi_n/q)(dq/d\psi_n)$ . The parameters  $\bar{v}_i = \bar{v}_e Q_i^2 Z_{\text{eff}} (m_e/m_i)^{1/2} (T_e/T_i)^{3/2}$  and  $\bar{v}_e = (4\pi n_e e^4 \ln \lambda) / ((2T_e)^{3/2} m_e^{1/2})$  determine the collision rates of ions and electrons (respectively) and are both normalized to  $v_{\text{th}i}/a$ . The quantity  $r$  is the half diameter of the flux surface across its midplane, while  $\rho_i$  is the Larmor radius of thermal ions.

$T_e$	592 eV	$v_e$	0.429
$T_i$	611 eV	$v_i$	0.0125
$a/L_{T_e}$	2.04	$\beta$	0.1
$a/L_{T_i}$	2.04	$q$	1.346
$n$	$4.36 \times 10^{19} \text{ m}^{-3}$	$\hat{s}$	0.286
$a/L_n$	-0.177	$r$	0.311 m
$P$	838 Pa	$\rho_i$	7.64 mm
$a/L_p$	1.87		

of this paper describes the equilibrium model we have considered and also the system of equations employed in the study of the micro-tearing mode. In section 3 the key features of the instability are discussed, including the sensitivity to temperature/density gradients, beta, collisionality, geometry, trapped particles and also the importance of the electrostatic potential and the ion response. These results confirm the micro-tearing modes found in MAST are not well described by the existing literature and reveal the processes that are crucial for instability. Our conclusions are given in section 4.

## 2. Plasma model

The plasma considered is MAST discharge #6252, which is a well-diagnosed Elmy H-mode plasma with neutral beam heating. An equilibrium reconstruction for this plasma has been calculated during a steady level of the plasma current and just before the neutral beams were switched off. (The key plasma parameters are listed in table 1, and a detailed discussion of the equilibrium calculation has been given in a previous publication [11].) In particular, we study the  $\psi_n = 0.4$  poloidal flux surface of this equilibrium ( $\psi_n = (\psi - \psi_{\text{min}}) / (\psi_{\text{max}} - \psi_{\text{min}})$  where  $\psi$  is the poloidal flux), since this was found to be highly susceptible to the micro-tearing mode. (The important plasma parameters for this surface are given in table 2). A significant difference between the plasma model employed here and that used in previous work [11] is the reduction in the number of kinetically modelled species from five to just two (main ions and electrons). This has significantly improved the tractability of our calculations without significantly affecting the results (see figure 1).

The linear gyrokinetic–Maxwell equations [15, 16] have been employed to study the micro-tearing instability present in this equilibrium. These equations provide a kinetic description

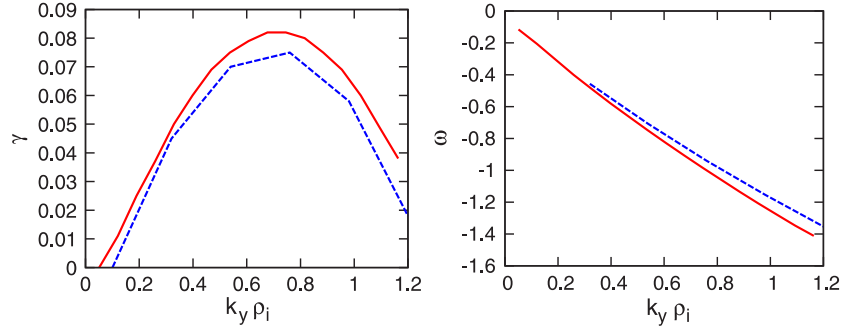


**Figure 1.** Growth rate ( $\gamma$ ) and real frequency ( $\omega$ ) of micro-tearing modes on the  $\psi_n = 0.4$  surface (both are normalized to  $v_{thi}/a$ ). These are plotted as functions of the normalized wave number  $k_y \rho_i$  (see appendix for the definition of the  $x$  and  $y$  coordinates used in GS2). The solid line represents the two species model, while the dashed line represents the five species model.

for the plasma in the limit

$$\frac{\omega}{\Omega} \approx \frac{k_{\parallel}}{k_{\perp}} \approx \frac{\rho}{L} \approx \delta \ll 1 \quad k_{\perp} \rho \sim 1 \quad (2)$$

where  $\Omega$  is the gyrofrequency,  $\omega$  is the oscillation frequency of the field perturbations,  $k_{\perp}$  and  $k_{\parallel}$  are the perpendicular and parallel numbers and  $L$  is the scale length of variations in the equilibrium distribution function. The linear gyrokinetic equation for a Fourier mode  $\mathbf{k}_{\perp}$  is given by the expression below.

$$\begin{aligned} \frac{\partial \hat{g}_{s,k_{\perp}}}{\partial t} + \mathbf{v}_{\parallel} \cdot \frac{\partial \hat{g}_{s,k_{\perp}}}{\partial \mathbf{R}} + \frac{1}{\Omega} \hat{\mathbf{z}} \times \left( \mu \frac{\partial B}{\partial \mathbf{r}} + v_{\parallel}^2 \hat{\mathbf{z}} \cdot \frac{\partial B}{\partial \mathbf{r}} \right) \cdot \frac{\partial \hat{g}_{s,k_{\perp}}}{\partial \mathbf{R}} \\ - \left( \frac{Q_s F_{0,s}}{T_s} \frac{\partial}{\partial t} + i \frac{\partial F_{0,s}}{\partial \mathbf{R}} \times \frac{\hat{\mathbf{z}}}{B} \cdot \mathbf{k}_{\perp} \right) \zeta_{k_{\perp}} = \mathcal{C}[\hat{g}_{s,k_{\perp}}], \end{aligned} \quad (3)$$

where  $\mathbf{R} = \mathbf{r} - (\hat{\mathbf{z}} \times \mathbf{v})/\Omega_s$  is the guiding centre coordinate, the nonadiabatic distribution function is given by  $g_s = \tilde{f}_s + (Q_s \phi F_{0,s}/T_s)$  (where  $Q_s$  is the particle charge,  $\phi$  is the electrostatic potential,  $\tilde{f}_s$  is the perturbed distribution function and  $F_{0,s}$  is the Maxwell–Boltzmann distribution function), finally  $\zeta_{k_{\perp}} = [\hat{\phi}_{k_{\perp}} J_0(z) - v_{\parallel} \hat{A}_{\parallel,k_{\perp}} J_0(z) + (v_{\perp}/|k_{\perp}|) \hat{B}_{\parallel,k_{\perp}} J_1(z)]$  where  $z = k_{\perp} v_{\perp}/\Omega$ . Particle collisions are modelled using a Lorentz collision operator:

$$\mathcal{C}[\hat{g}_{s,k_{\perp}}] = \frac{\nu_s(v)}{2} \left[ \frac{\partial}{\partial \xi} \Big|_{\mathbf{R}} (1 - \xi^2) \frac{\partial g_{s,k_{\perp}}}{\partial \xi} \Big|_{\mathbf{R}} - \frac{v^2(1 + \xi^2)}{2\Omega_s^2} k_{\perp}^2 g_{s,k_{\perp}} \right], \quad (4)$$

where  $\nu$  is the particle collision rate,  $\xi = v_{\parallel}/v$  is the pitch angle variable and  $|_{\mathbf{R}}$  denotes a partial derivative at constant  $\mathbf{R}$ . This operator calculates the pitch angle scattering of particles due to collisions, which enables an accurate model of trapped particle interactions. It also conserves energy and particle numbers. However it does not model the energy scattering involved in collisions and does not include momentum conservation. The diffusive term proportional to  $k_{\perp}^2$  is found to have little influence on the linear micro-tearing mode [12]. However, preliminary work suggests it may have a more important effect in nonlinear simulations of the instability [17]. Both ion–electron collisions and electron–electron collisions are included in the electron collision rate  $\nu_e(v)$ , while only ion–ion collisions are included in the ion collision

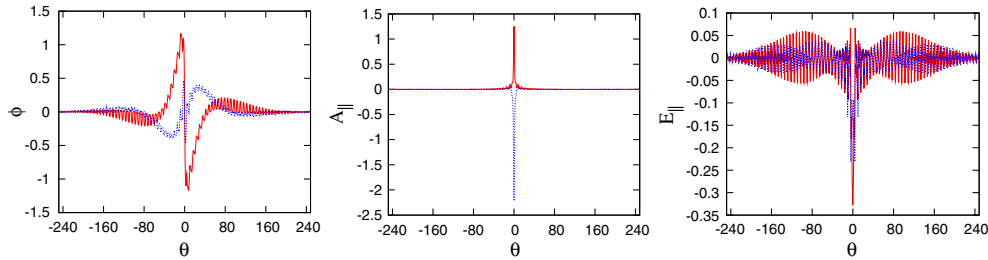


**Figure 2.** Eigenfunctions for the electrostatic potential  $\phi$ , the parallel vector potential  $A_{\parallel}$  and the parallel electric field  $E_{\parallel}$  plotted as functions of the ballooning angle  $\theta$ . The real part of each eigenfunction is represented by a solid line, whilst the imaginary parts are represented by dotted lines.

rate  $\nu_i(v)$ . However, it is found that electron–ion collisions are by far the most important of these collisional processes.

The gyrokinetic–Maxwell equations have been solved numerically using the initial value code GS2 [18]. This code assumes the equilibrium temperature and density scale lengths are constant across the radial simulation domain, and since the radial simulation domain is generally quite small for the micro-tearing instability in MAST, this approximation is reasonable (see [11]). Two further assumptions have also been made to improve the numerical tractability of these calculations. First the parallel magnetic perturbations ( $\tilde{\mathbf{B}}_{\parallel} = \nabla \times \mathbf{A}_{\perp}$ ) have been neglected, which, despite the high plasma  $\beta$ , have little effect on the micro-tearing mode (see section 3.8). Second, the plasma has been approximated as quasi-neutral. (Results obtained using the quasi-neutrality condition were found to be in good agreement with those obtained from Poisson’s equation.)

### 3. Results

Figure 2 is a plot of the parallel electric field  $\tilde{E}_{\parallel}$ , the electrostatic potential  $\tilde{\phi}$  and the parallel vector potential  $\tilde{A}_{\parallel}$  resulting from the micro-tearing instability at  $k_y \rho_i = 0.5$ . Each quantity is plotted as a function of the ballooning angle  $\theta$  (this labels distance along a magnetic field line using the poloidal angle). Importantly, the electrostatic potential and parallel electric field are highly extended along the field lines due to the rapid parallel motion of electrons. The parallel vector potential is confined to a much smaller range in  $\theta$ , which, in real space, produces a radially extended function. This corresponds to the ‘constant  $\psi$ ’ approximation of linear tearing theory [1].

The tearing nature of this instability becomes apparent when Poincaré sections are plotted of the perturbed magnetic field. In GS2 this is achieved using a flux tube simulation domain (see [19] for details), which is a long thin tube aligned parallel to the magnetic field lines. The parallel length extends from  $\theta = [-\pi, \pi]$  (as opposed to the ballooning representation where this domain can be arbitrarily large), while the perpendicular dimensions are a few Larmor radii. Parallel vector potential data from GS2 is then used to determine the path of selected magnetic field lines through the flux tube. Once these paths have been established, a perpendicular slice is taken through the tube at constant poloidal angle  $\theta$  and the points where the field lines intersect with this slice are plotted.

The Poincaré plots in figure 3 were produced using  $\tilde{A}_{\parallel}$  data for a single micro-tearing mode with wavenumber  $k_y \rho_i = 0.66$ . Each plot is given on an  $(x, y)$  grid, where  $x$  and  $y$  are the perpendicular coordinates in the flux tube, and are both normalized to the ion Larmor

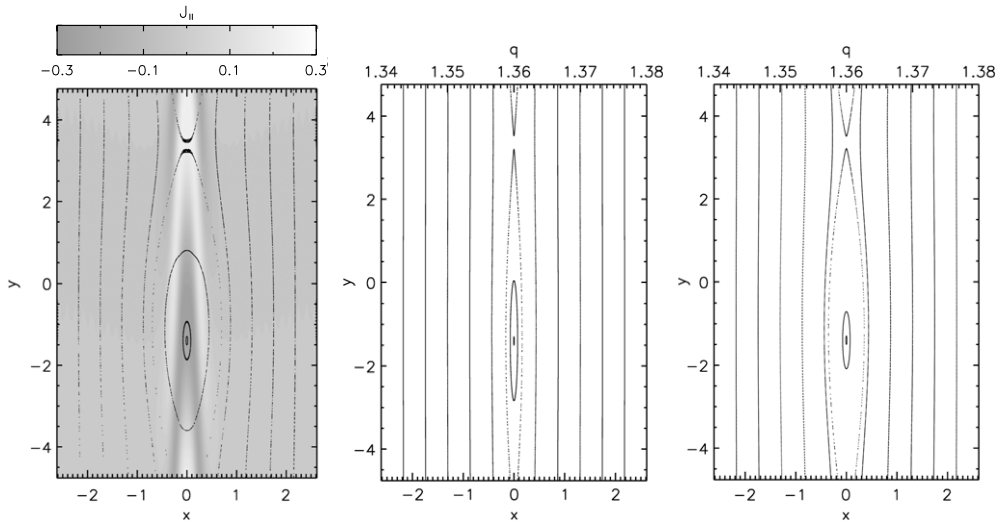


**Figure 3.** Poincaré plots for the micro-tearing instability with  $k_y \rho_i = 0.66$  at  $\theta = 0$ , where the  $x$  and  $y$  axes are given in units of  $\rho_i$ . The amplitude of the perturbation increases from left to right, so that the middle plot has a magnitude five times greater than the left-hand plot and four times smaller than the right-hand plot. The right-hand plot also includes a contour diagram of the parallel current  $\tilde{J}_{\parallel}$ .

radius  $\rho_i$ . (The definitions of  $x$  and  $y$  are given in the appendix.) A second horizontal axis labels the equivalent  $q$  values for the  $x$ -axis. Importantly, the field lines are tracked from the same starting points in each plot, while the amplitude of the magnetic field perturbation (due to the instability) increases from left to right. A magnetic island structure appears at the rational surface  $q = \frac{34}{25}$  of each plot which increases in size and complexity as the amplitude of the perturbation increases. The current plot in figure 3 reveals the ‘O’ point of the island is at the current minimum, whilst the ‘X’ point of the separatrix is at the current maximum. This current perturbation occurs in a narrow region around the resonant surface and corresponds to the current layer of linear tearing mode theory [1].

### 3.1. Drift-wave characteristics of the micro-tearing mode

The thermal force and trapped particle drive mechanisms for the micro-tearing instability both require a finite electron temperature gradient from which to draw free energy. The left-hand side of figure 4 is a plot of growth rate as a function of  $a/L_{Te}$  for the MAST micro-tearing instability with  $k_y \rho_i = 0.5$ . (Note, the ion temperature gradient was simultaneously altered to maintain a constant pressure gradient.) The instability is clearly dependent on the presence of a finite electron temperature gradient, as predicted by Hazeltine *et al* [2]. Further calculations have shown the growth rate also varies with the electron density gradient, although a finite density gradient is not vital to the instability.

Previous theories of the micro-tearing mode often predict a linear relation between the equilibrium electron temperature and density scale lengths and the real frequency of the mode. For example, the paper by Catto and Rosenbluth [9] predicts  $\omega \sim \omega_e^* [1 + \eta_e/2]$  (where  $\eta_e = (L_{n_e}/L_{Te})$ ), while numerical calculations by Gladd *et al* [20] produce real frequencies which roughly fit the expression,  $\omega \sim \omega_e^* [1 + [1 + 0.6 \ln(\bar{v}_e/\omega_e^*)] \eta_e]$ . Both these expressions have a qualitative agreement with calculations for the MAST instability (see figure 4 for

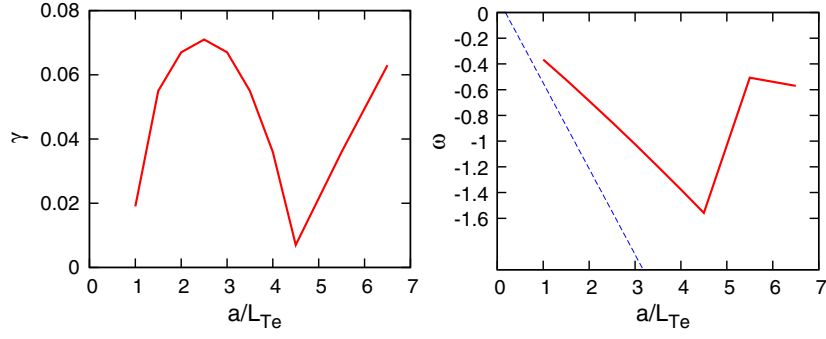


**Figure 4.** Growth rates and real frequency of micro-tearing modes as a function of the inverse electron temperature scale length  $a/L_{Te}$ . For comparison, the dashed line in the real frequency plot represents the analytic prediction  $\omega \sim \omega_e^* [1 + \eta_e/2]$ . Note that the inverse electron density scale length was kept constant, so  $\eta_e = L_n/L_T$  varies proportionally with  $a/L_{Te}$ .

the dependence of the real frequency on the electron temperature gradient). However, the frequency of the MAST instability also depends on the collision rate, which is closer to the predictions of Gladd *et al.*

Curiously there is a minimum in the growth rate of figure 4 at  $a/L_{Te} \approx 4.5$ , which coincides with a discontinuity in the frequency plot. This signifies a mode switching between two different micro-tearing instabilities, one which is unstable for  $0 < a/L_{Te} < 4.5$  (which we will call mode **A**), and another which is unstable for  $a/L_{Te} > 4.5$  (which we will call mode **B**). It is not obvious why mode **A** should be stabilized above  $a/L_{Te} \approx 4.5$  since the temperature gradient provides the free energy for the instability. A plausible explanation could be the dependence of the real frequency on the electron temperature gradient. If a resonance is important (for example, with the magnetic drift frequency), then increasing  $|\omega|$  may disturb this resonance and cause mode **A** to be damped. Interestingly,  $|\omega|$  sharply decreases across  $a/L_{Te} \sim 4.5$ . This means mode **B** has a real frequency similar to the real frequency of mode **A** at its most unstable and supports the idea that a lower  $|\omega|$  produces a destabilizing resonance in the plasma.

### 3.2. The role of collisions

It was discussed earlier that Drake and Lee [7] have defined three specific categories of tearing mode depending on the level of collisionality. However, it is not obvious which of these three categories the MAST micro-tearing instability belongs to. Consider figure 5, which shows the growth rate of the MAST micro-tearing instability as a function of collisionality. The instability is not collisionless, since the growth rate is clearly dependent on  $\bar{v}_e$ , and instability requires finite  $\bar{v}_e$  (figure 5). It is also not collisional or semi-collisional, since the collision rate is too low:  $0.05 \lesssim \bar{v}_e/\omega \lesssim 2$ . In fact, the instability seems to lie somewhere between the collisionless and semi-collisional regimes. Importantly, the MAST instability is unstable for  $\bar{v}_e \sim \omega$ . This regime has been addressed by Gladd *et al* [20] and D'Ippolito and Lee [21] using a modified Krook collision operator [22, 23]. Conversely, at lower collisionalities, the MAST instability is closer to the limit treated in the trapped particle calculations of Catto and Rosenbluth [9], where  $\omega > \bar{v}_e/\epsilon$ .

**3.2.1. The energy dependence of the collision operator.** Importantly, the thermal force drive mechanism of Hazeltine *et al* [2] and the trapped particle drive mechanism of Catto and

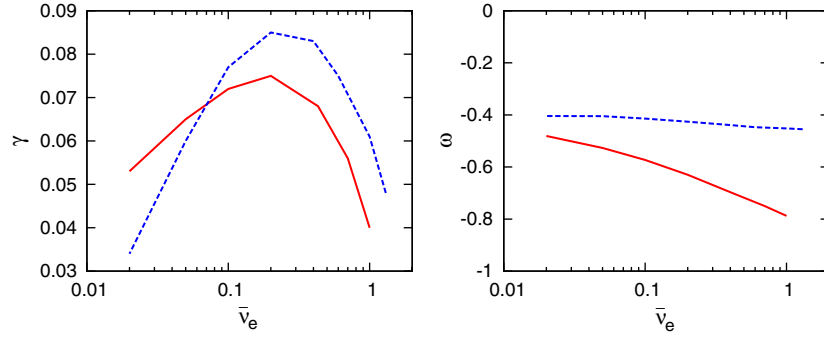


**Figure 5.** Plots of growth rate and real frequency for micro-tearing instabilities as a function of electron collisionality  $\bar{\nu}_e$ , for two different collision operators. The solid lines represent the energy dependent collision operator, while the dashed lines represent the energy independent collision operator from equation (5).

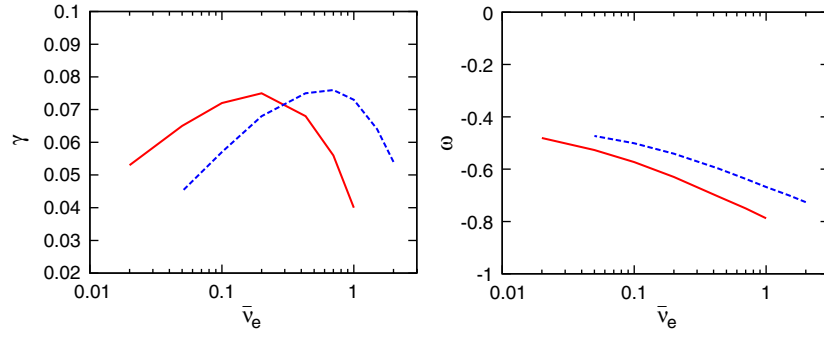


**Figure 6.** Plots of growth rate and real frequency versus collisionality for calculations with a full ion response (solid lines), and a Boltzmann response for the ions (dashed lines).

Rosenbluth [9] both require an energy dependent collision operator. Consequently we have tested whether the MAST instability is sensitive to the energy dependence of collisions. This test involved replacing the velocity/energy dependent collision rate of the electrons with the collision rate of electrons moving at their thermal velocity:

$$\nu_e(v) \rightarrow \nu_e(v_{th_e}). \quad (5)$$

Figure 5 is a plot of growth rate and real frequency versus the electron collisionality  $\bar{\nu}_e$ , using both the energy dependent collision operator and the energy independent collision operator. It is clear the instability is not strongly affected by the changed in collision operator, and thus cannot be strongly dependent on either of the drive mechanisms mentioned in the literature.

However, in the absence of magnetic drifts (see section 3.5) energy dependent collisions become more important to the MAST instability. This makes contact with the numerical calculations of Gladd *et al* [20] and D'Ippolitto and Lee [21], who find a micro-tearing instability in slab geometry, which is reliant on energy dependent collisions, and occurs in the regime  $\bar{\nu}_e \sim \omega$ .



### 3.3. The role of the ion response

The appropriate form for the ion response in tearing mode calculations has been widely discussed in the literature. Early calculations by authors such as Drake and Lee [7] utilize magnetized or unmagnetized approximations for the ion response, depending on the predicted width of the current layer  $d$  (a magnetized response is used if  $d \gg \rho_i$  while an unmagnetized response is used for  $d \ll \rho_i$ ). Later calculations by Cowley *et al* [8], implemented the effects of finite ion Larmor radius effects more completely, in the limit  $d < \rho_i$ . To discern the effect ion physics has on the MAST micro-tearing instability, a comparison has been made between calculations using the full ion response and calculations using an unmagnetized ion response:

$$\tilde{n}_i = -\frac{e\tilde{\phi}}{T_i} F_0, \quad (6)$$

where  $\tilde{n}_i$  is the perturbed ion density. The results of these calculations are presented in figure 6, where the growth rate and real frequency of the instability (at  $k_y \rho_i = 0.5$ ) are plotted against collision frequency. It is clear the full ion response has a limited influence on the instability, contrasting with the calculations of Cowley *et al* [8], who find FLR effects have a strong stabilising effect on the collisionless and semi-collisional tearing instabilities. However, this apparent contradiction can be explained by considering the current layer produced by the MAST micro-tearing instability. Figure 7 is a contour plot of the current perturbation produced by the  $k_y \rho_i = 0.5$  micro-tearing mode at  $\theta = 0$ . The current perturbation is concentrated in a small layer around  $x = 0$ , and here we define the width of this layer,  $d$ , using the following expression:

$$\frac{\int_{-d/2}^{d/2} |\tilde{J}_{\parallel}| dx dy}{\int_{-\infty}^{\infty} |\tilde{J}_{\parallel}| dx dy} = 0.75. \quad (7)$$

Figure 7 reveals  $d \sim \rho_i$  throughout the unstable collisional range, suggesting the approximation  $d < \rho_i$ , made by Cowley *et al* [8], is not applicable to the MAST instability. (In the limit  $d < \rho_i$  the current layer itself is largely unmagnetized, but the full ion response is still important outside the current layer. Indeed it is finite Larmor radius (FLR) effects *outside* of the current layer which Cowley *et al* find has a stabilizing effect on the instability. On the other hand, the MAST instability has  $d/\rho_i \sim 1$  so ion FLR effects ought to be important both inside and outside of the current layer.)

### 3.4. Micro-tearing instabilities in $s$ - $\alpha$ geometry

While numerical equilibria provide a realistic reconstruction of the experimental situation, they are somewhat inflexible when one wishes to modify equilibrium parameters. Thus, in order to study the effect that trapped particles, magnetic drifts and aspect ratio have on the micro-tearing instability, it is helpful to introduce an analytic equilibrium. Here we have constructed a shifted-circle,  $s$ - $\alpha$  equilibrium [24] where the flux surfaces are specified by

$$\begin{aligned} R &= R_0(r) + r \cos \theta, \\ Z &= r \sin \theta, \end{aligned} \quad (8)$$

where  $r$  is the minor radius of the flux surface,  $R$  and  $Z$  are the horizontal and vertical coordinates that specify the flux surface, and  $R_0(r)$  is the major radius of the flux surface (the

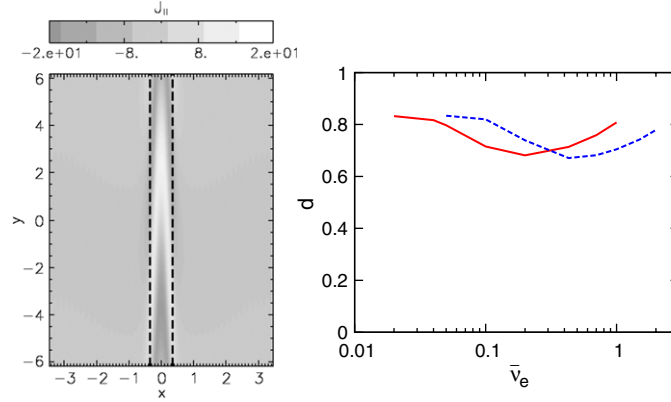


**Figure 7.** (Left) Cross section of the parallel current  $\tilde{J}_{\parallel}$  in the flux tube at  $\theta = 0$ , and at  $k_y \rho_i = 0.5$ . The dashed lines show the width  $d$  of the current layer which is defined in equation (7). (Right) The current width  $d$  is plotted as a function of collisionality  $\bar{v}_e$ , using full ion physics (solid line) and also a Boltzmann response for the ions (dashed line).

$s$ - $\alpha$  model allows this to be a function of the flux surface label  $r$ ). In this model the total magnetic drift velocity for electrons is given by

$$\mathbf{v}_R + \mathbf{v}_{\nabla B} = -\frac{2v_{\parallel}^2 + v_{\perp}^2}{2\Omega} \frac{\mathbf{R} \times \mathbf{B}}{R^2 B}. \quad (9)$$

Trapped particles can be included in the  $s$ - $\alpha$  model by using the following expression for the variation of the magnetic field strength:

$$B = \frac{B_0}{1 + \epsilon \cos(\theta)}, \quad (10)$$

where  $\epsilon = r/R_0$  is the inverse aspect ratio of the flux surface and controls the fraction of trapped particles.

In figure 8 the growth rates and real frequencies obtained using the  $s$ - $\alpha$  model are compared with those from the numerical MAST equilibrium. (This is only a rough comparison since the self consistency of the  $s$ - $\alpha$  model deteriorates at high  $\beta$  [25].) The same values of  $q$ ,  $\beta$ ,  $\hat{s}$ ,  $a/L_T$ ,  $a/L_n$ ,  $R_0$  and  $r/R_0$  are used in both models. It is clear the micro-tearing mode is unstable in the  $s$ - $\alpha$  equilibrium, suggesting the flux surface shaping of the MAST equilibrium is not particularly important for instability.

Using the  $s$ - $\alpha$  model, the major radius  $R_0$  and inverse aspect ratio  $\epsilon = r/R_0$  of a flux surface can be altered. In figure 8, the value of  $R_0$  has been changed keeping  $r$  fixed and allowing  $r/R_0$  to vary. Importantly, all other quantities, such as the temperature and density scale lengths, are kept constant. This is roughly equivalent to changing the aspect ratio  $R_0/a$  of a tokamak, whilst staying on the same flux surface  $r$ . From figure 8 it is clear that any increase in aspect ratio has a stabilizing effect on the micro-tearing instability, although it is also apparent the mode remains significantly unstable if the major radius is modestly increased. This in turn suggests the instability might appear in moderate aspect ratio machines such as JET (although it will be shown later on that the instability also requires a large  $\beta$ , which may prevent it from appearing at large aspect ratio).

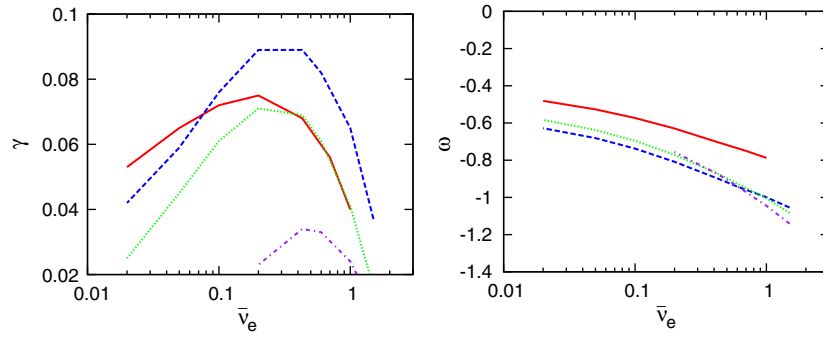


**Figure 8.** Growth rate and real frequency versus collisionality for four different plasma geometries. Calculations using the numerical reconstruction are given by solid lines. Results from the  $s$ - $\alpha$  model closest to this equilibrium (using  $r/R_0 = 0.345$  and  $R_0 = 0.879$ ) are given by dashed lines. The  $s$ - $\alpha$  calculations using  $r/R_0 = 0.236$  and  $R_0 = 1.32$  are given by dotted lines. Finally  $s$ - $\alpha$  results using  $r/R_0 = 0.118$  and  $R_0 = 2.64$  are given by dash-dot lines.

### 3.5. The effect of magnetic drifts

In the previous section an  $s$ - $\alpha$  model was utilized to vary  $R_0$  and  $\epsilon = r/R_0$  simultaneously. Consequently, both the magnetic drift velocity (which is inversely proportional to  $R_0$ ) and the trapped particle fraction (which is given by  $\epsilon^{1/2}$ ) were changed. In this section the  $s$ - $\alpha$  model is used to vary  $R_0$  while keeping  $\epsilon = r/R_0$  constant, allowing us to consider the effect of magnetic drifts in isolation.

The role that magnetic drifts play in the micro-tearing instability has not been fully treated in the literature. The majority of papers use either slab or cylindrical geometry to help tractability [2, 7, 8, 20], while a smaller number attempt to understand the role that trapped particles have on the instability [9, 10], but ignore the effects that curvature and  $\nabla B$  drifts have on untrapped electrons. Figure 9 compares the growth rates and real frequencies for calculations with a number of different major radii and with a range of collisionalities. These results show magnetic drifts have a significant destabilizing effect on the instability, and it is found that the destabilization comes predominantly via the untrapped electron species.

It is tempting to suggest the instability is driven by bad curvature at the outboard midplane of the tokamak, which is the destabilization mechanism for the toroidal ITG/ETG mode. However, in the case of the micro-tearing mode, the passing electrons must travel many poloidal orbits in an oscillation time of the mode ( $1/\omega$ ) and would be very sensitive to the average magnetic drift rather than just the bad curvature at the outboard midplane. Also, calculations have been performed where  $\alpha = -(2\mu_0 R q^2 / B^2)(dp/dr)$  has been increased in order to reduce the average curvature (this has been done inconsistently so that the driving gradients are kept constant). This was found to increase the growth rate of the micro-tearing instability, whereas bad curvature driven modes, such as the toroidal ITG mode, are expected to be stabilized. Thus, the destabilizing influence of magnetic drifts appears to be due to another process (perhaps a resonance between the mode frequency and the magnetic drift frequency as suggested in section 3.1).

The results from figure 9 show there is also an underlying slab drive mechanism for the micro-tearing instability in MAST, since the mode is unstable even when the magnetic drift velocity is zero. As we mentioned earlier, this additional mechanism appears to be closer to the slab calculations of Gladd *et al* [20], since the instability becomes much more sensitive to the energy dependence of the collision operator in the absence of magnetic drifts.

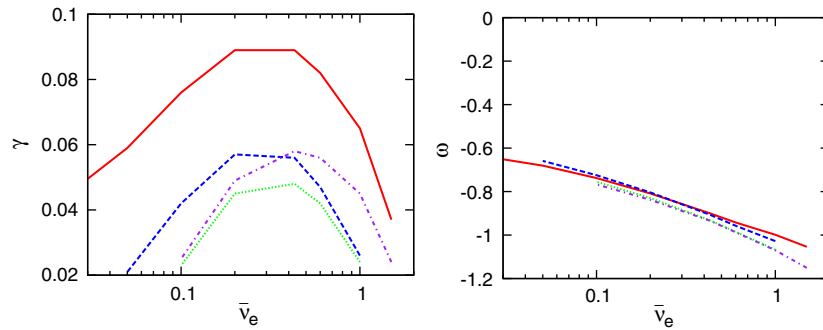


**Figure 9.** Plots of growth rate and real frequency versus collisionality using the  $s$ - $\alpha$  model with four different major radii at fixed inverse aspect ratio  $r/R_0$ . Solid lines represent  $R_0 = 0.879$ , dashed lines represent  $R_0 = 1.32$ , dotted lines represent  $R_0 = 2.64$ , dash-dot lines represent  $R_0 = \infty$  (i.e. cylindrical geometry). Note that  $k_y \rho_i = 0.5$  for all of these calculations.

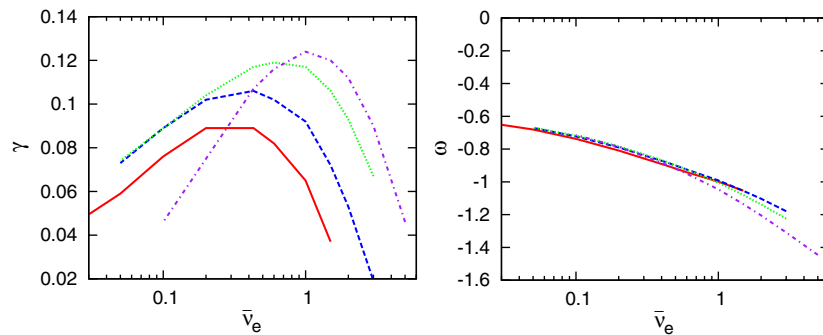


**Figure 10.** Plots of growth rate and real frequency versus collisionality using the  $s$ - $\alpha$  model with four different inverse aspect ratios  $r/R_0$  at fixed major radius  $R_0$ . Solid lines represent  $r/R_0 = 0.354$ , dashed lines represent  $r/R_0 = 0.236$ , dotted lines represent  $r/R_0 = 0.118$  and dot-dash lines represent  $r/R_0 = 0$ .

### 3.6. Calculations without trapped particles

It is also possible to investigate the role that trapped particles play in the micro-tearing instability using the  $s$ - $\alpha$  model. To do this we simply vary the ratio  $r/R_0$  whilst keeping  $R_0$  fixed. Figure 10 compares the growth rates and real frequencies of calculations with a number of different values of  $r/R_0$  and a range of collisionalities. Importantly these collision frequencies are well below the electron bounce frequency which is  $\omega_b = 12.6$  (all frequencies are normalized to  $v_{thi}/a$ ) so the banana orbits of trapped electrons are important.

Figure 10 reveals that the trapped particles are destabilizing at lower collision frequencies, which is in general agreement with the predictions of Catto and Rosenbluth [9]. It is also apparent that trapped particles are most destabilizing at smaller inverse aspect ratio, where the calculations of [9] are most accurate.

Importantly the trapped particles have a stabilizing effect at higher collision frequencies. This is probably because the trapped particles cannot respond to a parallel electric field, so in the absence of destabilizing boundary layer effects, the trapped particles will significantly reduce the perturbed current in the plasma and hence damp other drive mechanisms for the

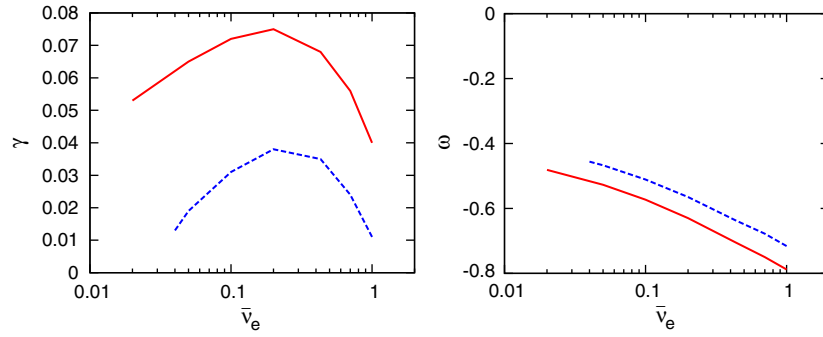


**Figure 11.** Plots of growth rate and real frequency as a function of collisionality. Solid lines include  $\tilde{\phi}$ , whilst the dashed lines have  $\tilde{\phi} = 0$ .

micro-tearing instability. Thus, we can see the stabilizing effect becomes stronger as the trapped particle fraction increases and is particularly strong for the aspect ratio of MAST.

### 3.7. The electrostatic potential

Gladd *et al* [20] find the electrostatic potential has a strong destabilizing influence on the micro-tearing instability when  $\omega \lesssim \bar{\nu}_e$ . The importance of the electrostatic potential has also been tested for the MAST micro-tearing instability by completing calculations with and without the electrostatic potential for a wide range of collisionalities (see figure 11). It is immediately apparent that the electrostatic potential has a strong destabilizing influence on the micro-tearing instability. Indeed if both the electrostatic potential and the magnetic drifts are turned off then the mode is stabilized.

### 3.8. The effect of $\beta$ and $\tilde{B}_{\parallel}$

Figure 12 presents a scan of growth rate versus total  $\beta$ . Two models of the plasma are compared, one including parallel magnetic perturbations ( $\tilde{B}_{\parallel}$ ) and one without. Importantly, these calculations keep  $\beta'$  and  $\nabla P$  constant while varying  $\beta$  (which is inconsistent), so the strength of magnetic perturbations in Ampère's law is varied, while the equilibrium is kept the same. The micro-tearing instability clearly requires a significant  $\beta$  value for instability. Below  $\beta \sim 0.1$  (which is the  $\beta$  value of the MAST equilibrium) the growth rate decreases rapidly. This is understandable since the lower values of  $\beta$  make it more difficult for the magnetic field to be perturbed. However, above  $\beta \sim 0.15$  the growth rate decreases again, which is not understood at present. Finally, we note that  $\tilde{B}_{\parallel}$  is unimportant to the micro-tearing instability, even at  $\beta \sim 0.4$ .

## 4. Conclusion

The tearing nature of the instability found in MAST has been confirmed by producing Poincaré plots of the perturbed magnetic field. These reveal chains of magnetic islands on the mode rational surfaces, and it is around these rational surfaces that most of the current perturbation lies in a 'current layer.' The centre of each island coincides with current minima, while the 'X' points coincide with current maxima, and the width of each magnetic island grows as the

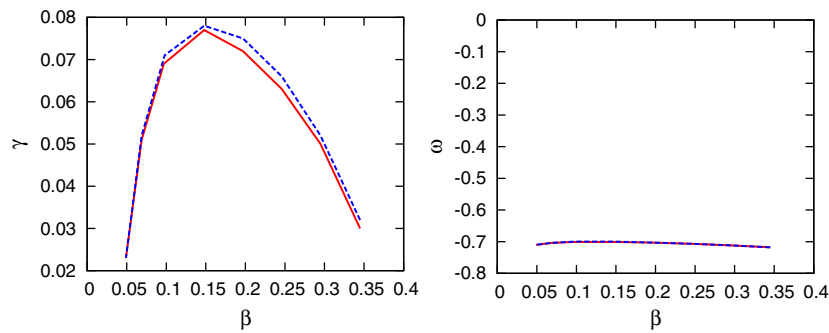


**Figure 12.** Plots of growth rate and real frequency versus plasma  $\beta$ . Solid lines include parallel magnetic perturbations, dashed lines do not.

amplitude of  $\tilde{A}_{\parallel}$  increases. These observations are in good agreement with linear tearing mode theory [1].

Previous work describes two different drive mechanisms for the micro-tearing instability. The first is due to the thermal force driving parallel currents in the plasma [2]. The second is caused by currents flowing in the collisional layers that form around the trapped–passing boundaries, whenever  $\bar{v}_e/\epsilon < \omega_c^*$  [9]. Both these mechanisms require an energy dependent collision operator, and both are dependent on a finite electron temperature gradient. Crucially, numerical studies in this paper have shown that neither drive mechanism is particularly important to the MAST instability, since the mode is largely unaffected when the energy dependence is removed from the collision operator. The trapped particle drive of Catto and Rosenbluth [9] appears to have a small destabilizing effect when  $\bar{v}_e/\epsilon < \omega$ , but there is clearly another drive mechanism for the micro-tearing instability that has not been described in the literature.

This new drive mechanism requires an electron temperature gradient from which to draw energy and has some dependence on the density gradient. The real frequency of the mode has a roughly linear dependence on both of these gradients, which suggests it has drift-wave-like properties. More detailed studies show the micro-tearing mode is strongly destabilized by magnetic drifts and the electrostatic potential. Indeed, if neither of these effects are included, then the MAST instability is completely stabilized.

The MAST micro-tearing mode is unstable in the collisional range  $0.05 \lesssim \bar{v}_e/\omega \lesssim 2$ . The lower end of this range pertains to the calculations of Catto and Rosenbluth [9] (which have already been mentioned), while the higher end of this range lies somewhere between the collisionless and semi-collisional regimes defined by Drake and Lee [7]. Importantly the collisional range of the MAST instability includes the collisional region  $\bar{v}_e \sim \omega$ , which Gladd *et al* [20] and D’Ippolito and Lee [21] have treated numerically. Nonetheless, despite treating the correct collisional range, these papers do not predict the MAST instability since they require an energy dependent collision operator for instability. However, if we remove magnetic drifts from our calculations then energy dependent collisions do become more important, thus making some contact with these earlier slab calculations [20, 21].

Importantly, it has been found that the exact form of the ion response has little effect on the MAST instability, despite the fact the current layer width  $d \sim \rho_i$ . Importantly, this does not conflict with previous calculations that include the full ion response [8], since these were performed in a different limit ( $d < \rho_i$ ).

Finally, the prevalence of the micro-tearing instabilities in simulations of the spherical tokamak is not due to its characteristic shaping, but rather it seems to be a result of the larger  $\beta$ , and the smaller radius of curvature in the ST (which provides stronger magnetic drifts).

### Acknowledgments

The authors would like to thank A Schekochihin, H R Wilson, M Redi and J F Drake for helpful discussions, and are thankful to N J Conway, A Patel and M J Walsh for contributing data from MAST. This work was funded jointly by the United Kingdom Engineering and Physical Sciences Research Council and by the European Communities under the contract of Association between EURATOM and UKAEA. The views and opinions expressed herein do not necessarily reflect those of the European Commission.

### Appendix. GS2 coordinates

GS2 uses a Clebsch representation for the magnetic field,

$$\mathbf{B} = \nabla\alpha \times \nabla\psi, \quad (12)$$

where  $\psi$  is the poloidal magnetic flux and  $\alpha = \phi - q\theta + v(\theta, \psi)$  labels different field lines on a flux surface. Thus,  $\psi$  and  $\alpha$  are two coordinates perpendicular to the field in the flux tube, while the distance along the field line is labelled using the poloidal angle  $\theta$ , which extends from  $\theta = (-\pi, \pi)$ . In GS2  $\alpha$  and  $\psi$  are transformed to  $x$  and  $y$  using

$$x = (\psi - \psi_0) \frac{q_0}{a B_a \rho}, \quad (13)$$

$$y = \alpha a \frac{d\psi_{\text{NORM}}}{d\rho}, \quad (14)$$

where  $a$  is the plasma minor radius,  $B_a$  is the vacuum magnetic field at the centre of the last closed flux surface,  $\psi_{\text{NORM}} = \psi/(a^2 B_a)$  and  $\rho_n$  is a normalized flux surface label increasing from zero at magnetic axis to one at the last closed flux surface. This results in a coordinate system  $(x, y, \theta)$ .

### References

- [1] Furth H P, Killeen J and Rosenbluth M N 1963 *Phys. Fluids* **6** 469
- [2] Hazeltine R D, Dobrott D and Tang T S 1975 *Phys. Fluids* **18** 1778
- [3] Roach C M, Akers R J, Conway N J, Dodge T M, Gryaznevich M P, Helander P, Sykes A, Walsh M J, the START Team and the NBI Team 2001 *Nucl. Fusion* **41** 11
- [4] Synakowski E J *et al* and the NSTX Research Team 2002 *Plasma Phys. Control. Fusion* **44** A165
- [5] Hassam A B 1980 *Phys. Fluids* **23** 2493
- [6] Braginskii S I 1965 *Reviews of Plasma Physics* vol 1 ed M A Leontovich (New York: Consultants Bureau)
- [7] Drake J F and Lee Y C 1977 *Phys. Fluids* **20** 1341
- [8] Cowley S C, Kulsrud R M and Hahm T S 1986 *Phys. Fluids* **29** 3230
- [9] Catto P J and Rosenbluth M N 1981 *Phys. Fluids* **24** 243
- [10] Connor J W, Cowley S C and Hastie R J 1990 *Plasma Phys. Control. Fusion* **32** 799
- [11] Applegate D J 2004 *Phys. Plasmas* **11** 5085
- [12] Roach C M *et al* and the MAST Team 2005 *Plasma Phys. Control. Fusion* **47** B323
- [13] Redi M H *et al* 2004 Nonlinear turbulence simulations for NSTX H-modes *31st EPS Conf. on Controlled Fusion and Plasma Physics (London)* number P2.162
- [14] Wilson H R *et al* 2004 *Nucl. Fusion* **44** 917
- [15] Taylor J B and Hastie R J 1968 *Plasma Phys.* **10** 479
- [16] Catto P 1977 *Plasma Phys.* **20** 719

- 
- [17] Applegate D J 2007 Gyrokinetic studies of a spherical tokamak H-mode plasma *PhD Thesis* University of London
- [18] Kotschenreuther M, Rewoldt G and Tang W M 1995 *Comput. Phys. Commun.* **88** 128
- [19] Beer M A, Cowley S C and Hammett G W 1995 *Phys. Plasmas* **2** 2687
- [20] Gladd N T, Drake J F, Chang C L and Liu C S 1980 *Phys. Fluids* **23** 1182
- [21] D'Ippolito D A and Lee Y C 1980 *Phys. Fluids* **23** 711
- [22] Williamson H 1968 *J. Phys. A: Math. Gen.* **1** 629
- [23] Bhatnagar P L, Gross E P and Krook M 1954 *Phys. Rev.* **94** 511
- [24] Connor J W, Hastie R J and Taylor J B 1979 *Phys. Rev. Lett.* **40** 396
- [25] Miller R L, Chu M S, Greene J M, Lin-Liu Y R and Waltz R E 1998 *Phys. Plasmas* **5** 973